Electronic Supplementary Material (ESI) for Physical Chemistry Chemical Physics.

Photo-induced structural dynamics of o-nitrophenol by Ultrafast Electron Diffraction

J. P. F. Nunes,[a†*] M. Williams,[bcd] J. Yang,[bce‡] T. J. A. Wolf,[c] C. D. Rankine,[f] R. Parrish,[b,c,d] B. Moore,[a] K. Wilkin,[a] X. Shen,[b] M. -F. Lin,[b] K. Hegazy,[cg] R. Li,[b‡] S Weathersby,[b] T. J. Martinez,[cd*] X. J. Wang,[b*] M. Centurion,[a*]

[a.] *Department of Physics and Astronomy, University of Nebraska-Lincoln, Lincoln, USA.*
[b.] *SLAC National Accelerator Laboratory, Menlo Park, USA.*
[c.] *Stanford PULSE Institute, SLAC National Accelerator Laboratory, Menlo Park, USA.*
[d.] *Department of Chemistry, Stanford University, Stanford, USA.*
[e.] *Center of Basic Molecular Science, Department of Chemistry, Tsinghua University, Beijing, China*
[f.] *School of Natural and Environmental Sciences, Newcastle University, UK.*
[g.] *Department of Physics, Stanford University, Stanford, USA.*
[†]Present address: Diamond Light Source Ltd, Didcot, UK.
[‡]Present address: Department of Engineering Physics, Tsinghua University, Beijing, China.

Electronic Supplementary Information

1. Ultrafast electron diffraction data processing

All diffraction patterns were processed using the following sequence of steps:

1) The detector baseline was removed by subtracting the mean value of the four corners (50×50 pixel area) outside the phosphor screen from the whole image.
2) For each image, pixels with an intensity five standard deviations over the mean and with the same *x* and *y* coordinates in the detector at the same time delay were removed.
3) Contributions from the hole in the detector (which allows the undiffracted electrons to pass through) and other detector artifacts (such as phosphor screen afterglow, or optical pump background) were removed using a mask.
4) The center of each diffraction pattern was determined independently by fitting circles to concentric intensity isolines. Diffraction patterns were realigned to a common center. The changes in diffraction pattern center were validated by comparison with the centroid of the undiffracted electron beam recorded by a second detector down the line.
5) For each image, pixels with an intensity six standard deviations over the mean at the same radial distance were removed.
6) A median filter with a 7×7 kernel size was applied to every image.
7) Diffraction patterns were normalized based on the mean counts between 1.5 and 5.5 $Å^{-1}$.

2. Ultrafast electron diffraction data reduction

Diffraction images were projected into Legendre polynomial form, reducing the data to one-dimensional intensity curves and allowing for the separation of isotropic and anisotropic contributions. In this approach, one-dimensional intensity curves are given by:

$$I_n(s) = \int P_n(\cos\phi) I(s,\phi) |\sin\phi| d\phi \tag{S1}$$

where P_n is the n^{th}-order Legendre polynomial, ϕ is the azimuthal angle in the diffraction image with respect to the direction of the laser polarization, $I(s,\phi)$ is the experimental scattering intensity, and s is the momentum transfer for the scattered electrons, defined as:

$$s = \frac{4\pi}{\lambda} \sin\left(\frac{\theta}{2}\right) \tag{S2}$$

where λ is the de Broglie wavelength of the incident electrons and θ is the angle between the incident and scattered electrons. The experimental conversion between detector pixels and momentum transfer was calibrated using the Bragg peak positions of a known single-crystal silica target. The $I_0(s)$ term in Eq. S1 encodes isotropic contributions to the total scattering, while higher-order Legendre polynomials reflect anisotropic contributions which arise from the preferential excitation of species with transition dipole moments parallel to the polarization of the pump laser.[1] No appreciable anisotropic contributions were found in our data, with higher-order Legendre polynomials showing negligible amplitudes. Therefore, our analysis focused exclusively on the 0^{th}-order $I_0(s)$ term, henceforth referred to simply as $I(s)$.

3. Simulation of static diffraction patterns

Simulated scattering signals – used (i) by the genetic structural fitting algorithm, and (ii) to compare the results of *ab initio* multiple spawning simulations with experimental data – were calculated under the independent atom model (IAM). Under this model, $I(s)$ can be expressed as the sum of the interference terms for all possible atom pairs, *i.e.* the molecular scattering, $I_{mol}(s)$, superimposed on the sum of the contributions from the atomic scattering, $I_{at}(s)$, for each atom in the sample:

$$I(s) = I_{mol}(s) + I_{at}(s) \tag{S3}$$

The atomic scattering term, defined in Eq. S4, does not contain structural information and can be easily calculated provided that the empirical formula of the target molecule is known.

$$I_{at}(s) = \sum_{i=1}^{N} f_i^*(s) f_i(s) \tag{S4}$$

In Eq. S4, $f_i(s)$ is the scattering amplitude of the i^{th} atom as calculated using the ELSEPA[2] program.

The molecular scattering term contains information on the internuclear separation of all atomic pairs in the molecule. In the case of an isotropic sample with N atoms, $I_{mol}(s)$ can be expressed as:

$$I_{mol}(s) = \sum_{i=1}^{N} \sum_{j=1, j \neq i}^{N} f_i^* f_j(s) \frac{\sin(sr_{ij})}{sr_{ij}} \tag{S5}$$

where r_{ij} is the distance between the i^{th} and the j^{th} atom. To compensate for the rapid drop in scattering intensity with increasing s imparted by the s^{-2} scaling in the elastic scattering amplitude f for each atom and the s^{-1} term in Eq. S5, diffraction data are typically presented as modified scattering intensities, $sM(s)$, defined as:

$$sM(s) = \frac{I_{\text{mol}}(s)}{I_{\text{at}}(s)} s \tag{S6}$$

$sM(s)$ curves enhance oscillations imparted by the $\sin(sr_{ij})/r_{ij}$ term in Eq. S5, thus making the comparison between experimental and simulated signals easier. Moreover, $sM(s)$ curves can be decomposed into a pair-distribution function (PDF) of the constituent interatomic distances using the following transform:

$$PDF(r) = \int_0^{s_{max}} sM(s) \sin(sr) e^{-ks^2} ds \tag{S7}$$

where r represents the interatomic distance, s_{max} is the maximum detectable momentum transfer in the diffraction pattern, and k is the damping factor used to minimize artifacts caused by the finite nature of the data and edge effects. For the steady-state PDFs, k = 0.03.

4. Determination of static pair-distribution-function from the experimental data

The experimental PDF is calculated by sine transformation of the experimental $sM(s)$, $sM_{\text{exp}}(s)$, using Eq. S7. $sM_{\text{exp}}(s)$ cannot be calculated directly using Eq. S6, however, as $I_{\text{mol}}(s)$ and $I_{\text{at}}(s)$ cannot be separated experimentally. Instead, an adaptation of the method developed by Ihee *et al*.[3] is used, where sM_{exp} (s) is expressed as:

$$sM_{exp}(s) = \frac{I_{\text{exp}}(s) - I_{bkg}}{I_{\text{at}}(s)} s \tag{S8}$$

with $I_{\text{exp}}(s)$ as the experimental scattering intensity and $I_{\text{bkg}}(s)$ as a smooth experimental background response which includes atomic scattering contributions and instrument-specific background. $I_{\text{bkg}}(s)$ is approximated by fitting a sum of exponents through s values corresponding to the zero-crossing of the simulated steady-state $I_{\text{mol}}(s)$ of o-nitrophenol.

5. Determination of difference signals – PD(s,t), ΔsM(s,t) and ΔPDF(r,t)

We employ the difference-diffraction method[4] to calculate the percentage difference (PD) signal, sometimes referred to as $\Delta I/I$, and difference sM(s,t) and PDF(r,t), ΔsM(s,t) and ΔPDF(r,t),

respectively. This method removes background and artifacts contributing to the diffraction signal by taking the difference between the diffraction signal at a delay time, t, and a reference signal recorded at a delay time $t < 0$. The PD, which is used in the genetic structural fitting algorithm, is defined as:

$$PD(s,t) = \frac{I(s,t) - I(s,t<0)}{I(s,t<0)} \tag{S9}$$

where $I(s,t)$ is the diffraction intensity recorded at some pump-probe delay time, t, and $I(s,t<0)$ is the reference signal taken at the delay time $t < 0$, *i.e.* before the arrival of the pump pulse. A low-order polynomial background is fitted to and subtracted from the PD signal in order to remove any background unaccounted for by the difference-diffraction method. The time-dependent difference pair distribution functions, $\Delta PDF(r,t)$, shown in the main text were calculated as:

$$\Delta PDF(r,t) = \int_0^{s_{max}} \Delta sM(s,t) \sin(sr) e^{-ks^2} ds \tag{S10}$$

where $\Delta sM(s,t)$ is the time-dependent difference-modified scattering curve, calculated as:

$$\Delta sM(s,t) = \frac{I(s,t) - I(s,t<0)}{I_{at}(s)} s \tag{S11}$$

The missing low-angle data, $\Delta sM(s<0.7,t)$, was filled in with linear extrapolation to $s = 0$. For the ΔPDFs, $k = 0.06$.

6. Determination of the signature of photodissociation and HONO release

The presence of signals consistent with photodissociation in the experimental UED signal was investigated by simulating the percentage difference (PD) and ΔPDF signal for C-N cleavage and HONO release and comparing those simulated signals against the average experimental PD and ΔPDF signal between 0.75 and 2 ps, shown in Fig. S1. In o-nitrophenol, photodissociation is characterized by a strong bleach of the PD signal at low scattering angle signal ($s<1$ Å^{-1}), shown in Fig. S1a. This photodissociation signature was not observed in the experimental PD.

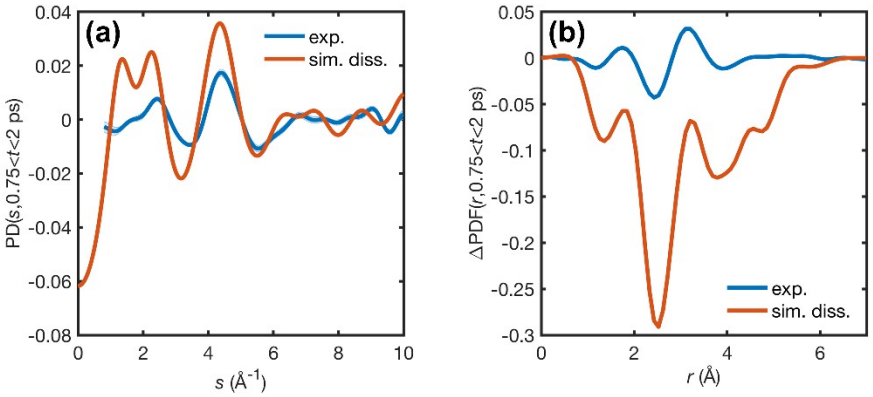

Fig. S1. Panel **(a)** shows the average experimentally measured (light blue) percentage difference (PD) signal between 0.75 and 2 ps and simulated PD signal for photodissociation and HONO release. Panel **(b)** shows the average experimentally measured (light blue) ΔPDF signal between 0.75 and 2 ps and simulated ΔPDFs signal for photodissociation and HONO release.

7. Temporal evolution of the real-space features

The relative evolution of real-space features is highlighted by experimental and simulated ΔPDFs lineouts along the peaks β and γ (see main text for definition) shown in Fig. S2a and S2b, respectively. Both experimental and simulated lineouts show two different timescales for the depletion of peak β and rise of peak γ. The experimental signal for peak β depletes in 560±241 fs full-width-half-maximum (FWHM) centered at 591±78 fs. This is slower and later than the rise of peak γ which exhibits an onset of 347±132 fs FWHM centered at 522±40 fs. Despite the difference in nominal timescale, AIMS simulations corroborate this observation, with the peak β (119±4 fs FWHM centered at 205±1 fs) showing a slighter delayed and slower depletion relative to the rise of peak γ (67±13 fs FWHM centered at 161±4 fs).

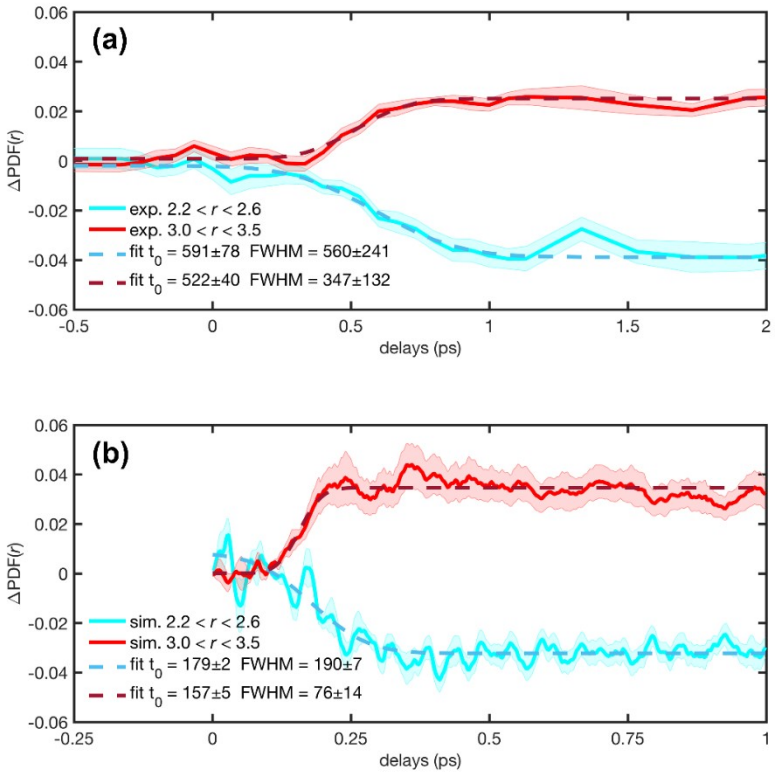

Fig. S2 Panels **(a)** and **(b)** shows the experimental and simulated time evolution of the area under regions β (2.2-2.6 Å, blue) and γ (3.0-3.5 Å, light red) and corresponding fits, respectively. Uncertainties are shown as shaded regions, which represent one standard deviation confidence interval obtained from bootstrap analysis in the case of experimental data, and reflect the convergence obtained from the initial conditions in the case of simulated observables.

8. Structure determination by genetic structure fitting algorithm

A genetic structural fitting algorithm (GSFA) was used to retrieve structural information from the scattering signal directly. A similar method was developed by Habershon and Zewail[5] to determine reaction end products and, more recently, employed by Yang *et al.* to identify the ring puckering of photoexcited pyridine.[6] In our implementation, o-nitrophenol is described by a geometric model with 39 structural parameters: 14 interatomic distances, 13 angles, and 12 dihedral angles. These structural parameters are constrained according to the boundaries shown in Table S1. The atom numbering used in Table S1 is clarified in Fig. S3.

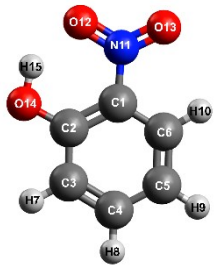

Fig. S3 Ground-state geometry of o-nitrophenol overlaid with the atom numbering used in the genetic structural fitting algorithm geometric model.

Table S1 List of parameters and constraints used in the genetic structural fitting algorithm geometric model.

Parameters	S_0 eq. value	Lower bound constraint	Upper bound constraint
rC_1C_2	1.415	1.200	1.600
rC_2C_3	1.404	1.200	1.600
rC_3C_4	1.382	1.200	1.600
rC_4C_5	1.404	1.200	1.600
rC_5C_6	1.380	1.200	1.600
rC_3H_7	1.083	1.029	1.137
rC_4H_8	1.084	1.029	1.138
rC_5H_9	1.082	1.028	1.136
rC_6H_{10}	1.081	1.027	1.135
rC_1N_{11}	1.453	1.000	1.650
rC_2O_{14}	1.337	1.000	1.650
$rN_{11}O_{12}$	1.248	1.000	1.400
$rN_{11}O_{13}$	1.219	1.000	1.400
$rO_{12}H_{15}$	0.954	0.850	1.400
$\angle C_1C_2C_3$	117.7	100.0	140.0
$\angle C_2C_3C_4$	120.8	100.0	140.0
$\angle C_3C_4C_5$	121.0	100.0	140.0
$\angle C_4C_5C_6$	119.4	100.0	140.0
$\angle H_7C_3C_4$	121.6	115.5	127.7
$\angle H_8C_4C_5$	119.8	113.8	125.8
$\angle H_9C_5C_6$	120.1	114.1	126.1
$\angle H_{10}C_6C_1$	118.3	112.4	124.2
$\angle N_{11}C_1C_2$	120.8	100.0	140.0
$\angle O_{14}C_2C_3$	117.7	100.0	140.0
$\angle O_{12}N_{11}C_1$	117.9	100.0	140.0
$\angle O_{13}N_{11}O_{12}$	122.8	100.0	140.0
$\angle H_{15}O_{12}N_{11}$	104.5	90.00	180.0
$\angle C_1C_2C_3C_4$	360.0	300.0	420.0
$\angle C_2C_3C_4C_5$	360.0	300.0	420.0
$\angle C_3C_4C_5C_6$	360.0	300.0	420.0
$\angle H_7C_3C_4C_5$	180.0	171.0	189.0
$\angle H_8C_4C_5C_6$	180.0	171.0	189.0
$\angle H_9C_5C_6C_1$	180.0	171.0	189.0
$\angle H_{10}C_6C_1C_2$	180.0	171.0	189.0
$\angle N_{11}C_1C_2C_3$	180.0	90.0	270.0
$\angle O_{14}C_2C_3C_4$	180.0	90.0	270.0
$\angle O_{12}N_{11}C_1C_2$	0.0	0.0	360.0
$\angle O_{13}N_{11}O_{12}C_1$	180.0	135.0	225.0
$\angle H_{15}O_{12}N_{11}C_1$	180.0	0.0	360.0

The GSFA retrieval was initiated with a pool of 1000 structures, each defined by 39 parameters with their values chosen at random within the constraint boundaries. The fitness of each structure was evaluated according to the χ^2 value between the experimental and simulated PD:

$$\chi^2 = \sum_{s_{min}}^{s_{max}} \left(\frac{PD_{exp}(s,t) - PD_{sim}(s,t)}{\sigma_{exp}(s,t)} \right)^2 \tag{S12}$$

where $\sigma_{exp}(s,t)$ is the experimental uncertainty value for the PD signal and $PD_{exp}(s,t)$ and $PD_{sim}(\underline{s},t)$ are the experimental and simulated PD signals, respectively. $PD_{sim}(s,t)$ was calculated using the ground-state equilibrium geometry of o-nitrophenol as a reference and assumed a fixed excitation percentage. A preliminary GSFA run on the average difference scattering signal for $t >$ 5 ps was used to estimate the excitation percentage by adding a scaling factor as a fitting parameter. This scaling factor was found to be 0.1675 and was fixed in all subsequent uses of the GSFA. Fig. S4 shows a comparison between $PD_{exp}(s,t)$ and $PD_{sim}(\underline{s},t)$ for the best-fitting structures at a range of time delays. Note the good agreement between the experimental and GSFA-retrieved difference scattering signals.

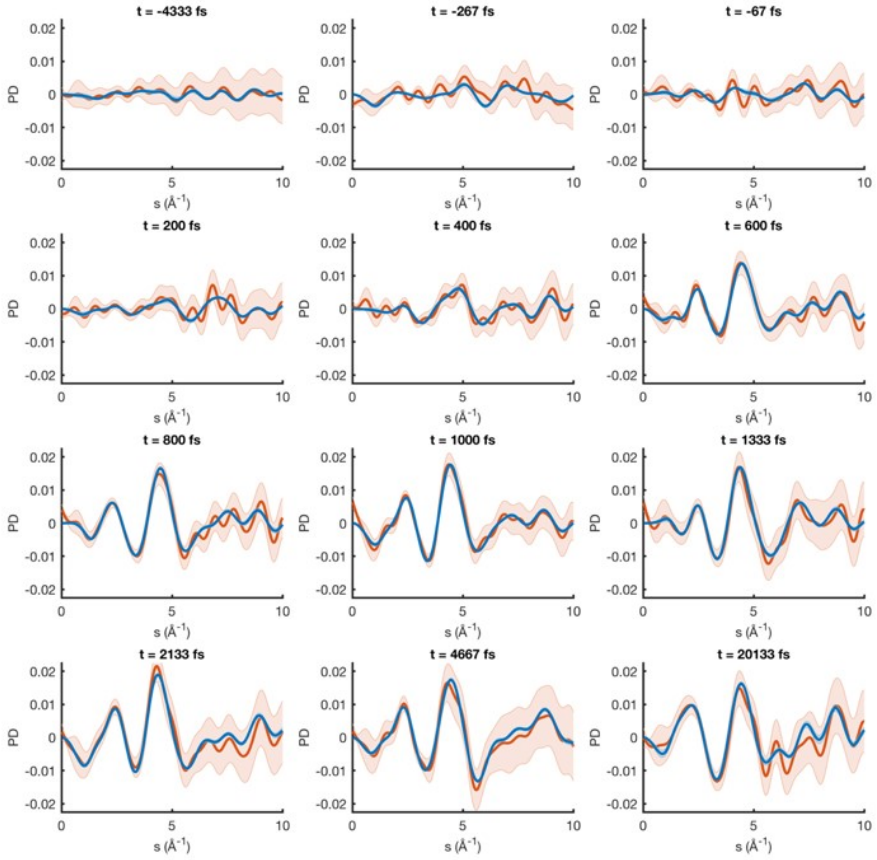

Fig. S4 Plots of experimental (red) and computed (blue) PD with the lowest χ^2 for different time delays. These plots show good agreement between the experimental and retrieved PD. The

shaded areas in the experiment represent a 68% confidence interval obtained from bootstrap analysis of the experimental data.

A diagram of the GSFA is shown in Fig. S5. Briefly, following the initialization with 1000 random structures and χ^2 evaluation, the 50 structures with the lowest χ^2 value are selected as parents for the next generation of structures. In each generation, child populations of 1000 structures are produced by 80% crossover and 20% mutation of the selected parent population. A heuristic approach is used in the crossover step by which the parameters of a child structure lie on a hypothetical line between two parents at a smaller distance from the parent with the best fitness value. The heuristic crossover operator can be described for a given parameter, *i*, as:

$$i_{child} = i_{best\ parent} + a(i_{best\ parent} - i_{worst\ parent}) \quad \text{(S13)}$$

In our implementation of the heuristic crossover operator, *a* was set to 1.2. This approach uses the fitness of the parents to dictate the direction in which the population should evolve, thereby speeding up convergence. The GSFA was run for a maximum of 100 generations for each time delay. In cases where the overall fitness function did not improve for more than 25 consecutive generations, the run was terminated. The GSFA was repeated 75 times for each of the 37 time delays, thus allowing a bootstrap analysis of the uncertainty on the retrieved internal coordinates. The results of the GSFA are summarized in Tables S2, S3, and S5.

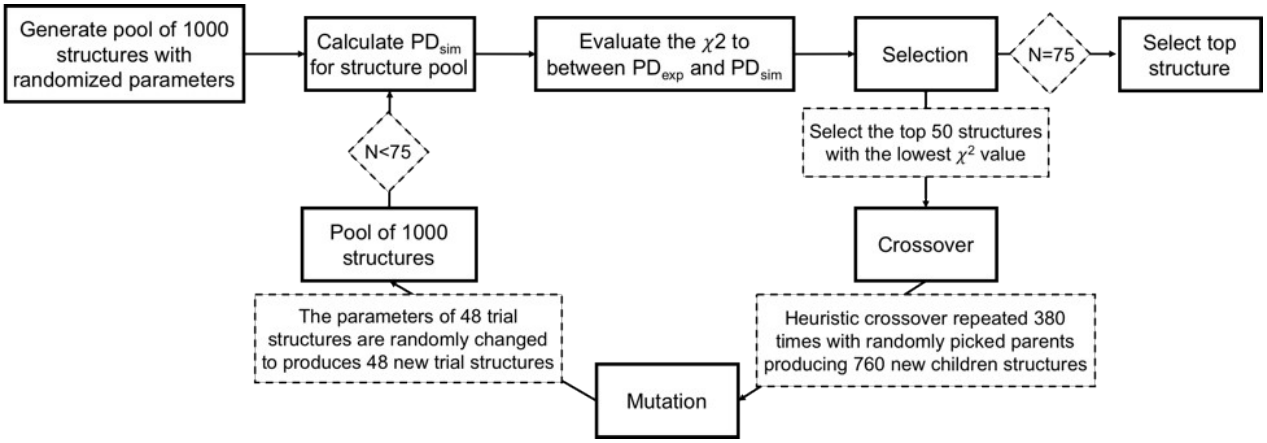

Fig. S5 Flowchart of the genetic structural fitting algorithm.

Table S2 Genetic structural fitting results for distances. Uncertainty is calculated using one standard deviation of individual fitting results.

Time / fs	rC_1C_2	rC_2C_3	rC_3C_4	rC_4C_5	rC_5C_6	rC_3H_7	rC_4H_8	rC_5H_9	rC_6H_{10}	rC_1N_{11}	rC_2O_{14}	$rN_{11}O_{12}$	$rN_{11}O_{13}$	$rO_{12}H_{15}$
-4333	1.41±0.02	1.41±0.03	1.39±0.02	1.43±0.02	1.39±0.02	1.14±0.00	1.09±0.02	1.14±0.00	1.14±0.00	1.46±0.02	1.32±0.02	1.20±0.02	1.25±0.02	0.87±0.02
-4267	1.42±0.01	1.41±0.01	1.38±0.01	1.41±0.01	1.40±0.02	1.04±0.01	1.04±0.01	1.13±0.01	1.08±0.02	1.46±0.01	1.32±0.02	1.25±0.01	1.21±0.01	0.97±0.02
-333	1.42±0.02	1.48±0.01	1.33±0.02	1.38±0.02	1.28±0.02	1.13±0.02	1.14±0.00	1.03±0.00	1.08±0.04	1.39±0.02	1.30±0.02	1.20±0.01	1.33±0.02	1.22±0.06
-267	1.42±0.02	1.45±0.03	1.36±0.03	1.43±0.04	1.32±0.04	1.14±0.00	1.14±0.00	1.04±0.03	1.14±0.00	1.42±0.03	1.28±0.02	1.20±0.01	1.26±0.03	1.34±0.12
-200	1.45±0.03	1.42±0.04	1.39±0.04	1.44±0.04	1.34±0.02	1.14±0.00	1.14±0.00	1.14±0.00	1.14±0.00	1.44±0.02	1.28±0.02	1.21±0.01	1.22±0.02	1.11±0.03
-133	1.43±0.02	1.42±0.03	1.38±0.03	1.42±0.02	1.33±0.03	1.14±0.00	1.14±0.00	1.13±0.02	1.13±0.01	1.44±0.02	1.22±0.02	1.19±0.02	1.27±0.02	1.04±0.02
-67	1.41±0.03	1.36±0.03	1.39±0.03	1.39±0.03	1.39±0.03	1.06±0.03	1.14±0.00	1.08±0.03	1.14±0.00	1.51±0.03	1.29±0.02	1.24±0.02	1.19±0.01	1.17±0.10
0	1.41±0.03	1.39±0.04	1.39±0.02	1.40±0.02	1.38±0.04	1.05±0.04	1.13±0.02	1.03±0.00	1.14±0.00	1.44±0.03	1.34±0.03	1.25±0.01	1.27±0.02	1.12±0.05
67	1.44±0.03	1.42±0.03	1.40±0.03	1.41±0.03	1.39±0.02	1.14±0.00	1.14±0.00	1.13±0.01	1.14±0.00	1.39±0.03	1.32±0.02	1.25±0.01	1.25±0.01	0.85±0.00
133	1.41±0.03	1.42±0.03	1.41±0.03	1.41±0.03	1.39±0.03	1.13±0.01	1.03±0.00	1.09±0.05	1.13±0.01	1.37±0.03	1.28±0.02	1.25±0.02	1.27±0.02	1.00±0.08
200	1.41±0.02	1.40±0.03	1.39±0.03	1.40±0.03	1.36±0.03	1.13±0.01	1.03±0.00	1.14±0.00	1.07±0.04	1.42±0.03	1.30±0.02	1.22±0.01	1.26±0.02	1.09±0.07
267	1.41±0.02	1.36±0.03	1.40±0.04	1.39±0.03	1.30±0.05	1.14±0.00	1.14±0.00	1.14±0.00	1.13±0.00	1.44±0.02	1.27±0.03	1.21±0.02	1.33±0.02	0.98±0.01
333	1.43±0.03	1.35±0.06	1.38±0.07	1.41±0.03	1.35±0.04	1.12±0.04	1.14±0.00	1.14±0.00	1.13±0.02	1.44±0.02	1.31±0.05	1.21±0.03	1.33±0.05	0.95±0.02
400	1.43±0.03	1.36±0.06	1.40±0.06	1.39±0.04	1.39±0.04	1.09±0.05	1.04±0.02	1.13±0.01	1.06±0.04	1.47±0.03	1.36±0.05	1.27±0.04	1.25±0.04	1.08±0.11
467	1.44±0.04	1.40±0.05	1.38±0.06	1.39±0.05	1.38±0.09	1.10±0.04	1.04±0.01	1.08±0.04	1.09±0.04	1.48±0.05	1.34±0.06	1.24±0.07	1.24±0.06	1.25±0.13
533	1.42±0.05	1.39±0.06	1.39±0.07	1.37±0.08	1.36±0.10	1.10±0.04	1.04±0.01	1.09±0.04	1.05±0.03	1.50±0.07	1.40±0.08	1.30±0.06	1.28±0.05	1.05±0.10
600	1.43±0.06	1.42±0.08	1.38±0.08	1.41±0.09	1.39±0.09	1.07±0.05	1.07±0.05	1.07±0.05	1.04±0.03	1.47±0.05	1.44±0.10	1.29±0.07	1.27±0.08	1.11±0.24
667	1.43±0.06	1.44±0.04	1.40±0.06	1.42±0.05	1.40±0.07	1.12±0.04	1.13±0.01	1.08±0.05	1.09±0.05	1.44±0.05	1.42±0.08	1.20±0.13	1.18±0.12	1.08±0.24
733	1.43±0.06	1.42±0.06	1.41±0.07	1.43±0.05	1.43±0.06	1.12±0.04	1.07±0.04	1.10±0.04	1.10±0.04	1.42±0.07	1.41±0.10	1.20±0.12	1.20±0.12	1.14±0.21
800	1.42±0.06	1.42±0.07	1.39±0.07	1.42±0.06	1.42±0.06	1.08±0.04	1.04±0.02	1.05±0.04	1.11±0.04	1.42±0.07	1.45±0.06	1.21±0.07	1.23±0.08	1.12±0.16
867	1.44±0.07	1.43±0.06	1.41±0.07	1.42±0.06	1.43±0.07	1.12±0.03	1.12±0.03	1.10±0.04	1.11±0.04	1.38±0.07	1.42±0.08	1.19±0.05	1.18±0.04	1.23±0.08
933	1.43±0.08	1.45±0.06	1.41±0.08	1.40±0.08	1.43±0.09	1.11±0.04	1.13±0.01	1.11±0.04	1.10±0.04	1.41±0.07	1.45±0.12	1.20±0.04	1.19±0.02	1.23±0.08
1000	1.45±0.08	1.46±0.07	1.39±0.09	1.38±0.09	1.40±0.11	1.09±0.05	1.08±0.04	1.08±0.05	1.08±0.05	1.45±0.09	1.47±0.10	1.25±0.04	1.25±0.04	1.05±0.19
1067	1.42±0.08	1.44±0.08	1.38±0.09	1.41±0.09	1.40±0.10	1.06±0.04	1.10±0.05	1.05±0.04	1.08±0.05	1.49±0.10	1.49±0.13	1.27±0.04	1.28±0.04	0.89±0.11
1133	1.44±0.10	1.43±0.11	1.38±0.11	1.40±0.12	1.43±0.12	1.07±0.05	1.07±0.05	1.06±0.04	1.07±0.05	1.55±0.12	1.47±0.16	1.27±0.03	1.27±0.04	0.92±0.17
1333	1.44±0.07	1.43±0.08	1.41±0.09	1.41±0.07	1.45±0.07	1.11±0.03	1.06±0.04	1.12±0.03	1.09±0.04	1.46±0.07	1.34±0.12	1.20±0.08	1.23±0.07	1.06±0.14
1533	1.44±0.10	1.42±0.11	1.42±0.09	1.40±0.10	1.42±0.11	1.10±0.05	1.09±0.05	1.10±0.05	1.06±0.04	1.45±0.12	1.46±0.14	1.24±0.13	1.22±0.14	1.17±0.23
1733	1.46±0.09	1.42±0.08	1.45±0.09	1.40±0.10	1.42±0.10	1.07±0.05	1.13±0.02	1.05±0.04	1.07±0.05	1.42±0.13	1.36±0.15	1.19±0.10	1.22±0.08	1.00±0.21
1933	1.47±0.06	1.45±0.06	1.39±0.09	1.37±0.09	1.40±0.07	1.08±0.05	1.07±0.05	1.07±0.04	1.07±0.05	1.47±0.07	1.32±0.14	1.23±0.11	1.18±0.10	0.96±0.21
2133	1.45±0.11	1.42±0.11	1.43±0.10	1.36±0.09	1.44±0.09	1.03±0.00	1.03±0.00	1.03±0.00	1.03±0.01	1.46±0.12	1.46±0.14	1.34±0.04	1.32±0.05	0.85±0.00
2667	1.45±0.13	1.42±0.11	1.42±0.12	1.42±0.12	1.44±0.13	1.07±0.05	1.08±0.05	1.06±0.05	1.04±0.03	1.48±0.16	1.43±0.16	1.29±0.03	1.28±0.03	1.12±0.25
3667	1.46±0.04	1.45±0.04	1.41±0.05	1.39±0.04	1.40±0.04	1.06±0.04	1.05±0.03	1.04±0.02	1.12±0.03	1.39±0.05	1.43±0.04	1.19±0.10	1.21±0.10	1.03±0.19
4667	1.45±0.07	1.40±0.09	1.43±0.08	1.43±0.08	1.43±0.07	1.10±0.05	1.13±0.03	1.09±0.05	1.09±0.05	1.46±0.07	1.42±0.11	1.17±0.13	1.11±0.12	1.19±0.22
5667	1.46±0.05	1.47±0.08	1.40±0.07	1.40±0.06	1.40±0.08	1.06±0.04	1.04±0.02	1.05±0.04	1.06±0.04	1.41±0.08	1.46±0.07	1.20±0.08	1.24±0.08	1.02±0.21
10133	1.44±0.07	1.44±0.06	1.40±0.08	1.41±0.07	1.44±0.06	1.08±0.05	1.11±0.04	1.08±0.05	1.08±0.05	1.50±0.06	1.35±0.15	1.19±0.15	1.19±0.16	1.06±0.26
20133	1.45±0.03	1.41±0.03	1.40±0.05	1.39±0.06	1.39±0.06	1.12±0.04	1.12±0.04	1.11±0.05	1.09±0.05	1.45±0.03	1.42±0.02	1.13±0.14	1.18±0.14	1.21±0.21

Table S3 Genetic structural fitting results for angles. Uncertainty is calculated using one standard deviation of individual fitting results.

Time / fs	$\angle C_1C_2C_3$	$\angle C_2C_3C_4$	$\angle C_3C_4C_5$	$\angle C_4C_5C_6$	$\angle H_7C_3C_4$	$\angle H_8C_4C_5$	$\angle H_9C_5C_6$	$\angle H_{10}C_6C_1$	$\angle N_{11}C_1C_2$	$\angle O_{14}C_2C_3$	$\angle O_{12}N_{11}C_1$	$\angle O_{13}N_{11}O_{12}$	$\angle H_{15}O_{12}N_{11}$	$\angle C_1C_2C_3$
-4333	116±2	121±1	121±1	118±2	124±4	124±3	117±2	113±1	122±2	120±1	119±1	128±2	124±8	116±2
-4267	118±1	120±1	121±1	120±1	117±2	124±4	126±1	123±2	119±1	117±1	116±1	125±2	112±3	118±1
-333	118±1	120±1	124±1	121±1	124±2	123±2	115±2	117±3	122±1	122±1	117±1	122±2	127±2	118±1
-267	117±1	119±1	125±1	123±2	127±1	124±2	114±0	113±2	121±1	126±1	120±1	115±1	122±3	117±1
-200	117±2	120±2	121±2	123±2	120±2	125±1	115±2	113±1	119±2	127±2	122±2	112±4	97±4	117±2
-133	118±2	120±2	120±2	124±2	117±1	125±1	124±3	114±2	121±1	124±1	120±2	117±2	91±2	118±2
-67	119±2	122±2	118±2	122±2	127±2	120±3	118±5	118±2	117±2	124±2	120±2	123±3	94±5	119±2
0	121±2	121±2	122±2	119±2	128±0	119±5	114±0	122±3	121±2	129±3	121±2	121±2	98±4	121±2
67	122±2	120±2	123±2	119±2	125±2	119±3	114±0	122±2	123±2	131±2	120±2	121±3	106±10	122±2
133	120±2	121±2	121±2	119±3	122±4	118±5	117±4	117±5	126±3	120±3	116±3	118±2	108±5	120±2
200	120±2	123±2	120±2	120±2	122±5	119±6	123±5	113±2	123±2	120±2	117±3	119±2	108±7	120±2
267	118±2	125±2	118±3	121±3	120±6	125±2	118±6	112±0	123±2	124±2	122±5	125±3	90±0	118±2
333	119±2	126±5	114±5	125±5	126±4	125±1	123±5	114±3	123±2	125±4	118±5	123±3	91±1	119±2
400	120±4	122±4	117±4	123±5	123±5	125±1	126±0	116±5	125±3	122±4	115±4	121±3	93±4	120±4
467	119±3	120±4	118±4	121±5	120±6	119±6	123±5	118±5	124±5	125±5	113±7	127±7	92±5	119±3
533	118±4	119±4	119±4	120±7	121±5	121±6	125±2	117±6	122±4	117±4	121±4	116±9	98±8	118±4
600	119±7	119±7	118±5	117±7	120±5	122±5	124±4	120±5	119±6	115±7	122±6	114±11	136±29	119±7
667	117±6	119±6	117±5	119±7	120±5	123±4	121±5	120±5	120±8	119±9	125±9	107±12	108±20	117±6
733	120±8	119±7	116±8	119±9	122±5	120±5	121±5	119±5	120±9	118±10	124±11	113±15	117±25	120±8
800	117±7	120±7	119±7	116±8	125±4	121±6	118±5	119±5	121±9	120±8	122±11	110±12	105±16	117±7
867	117±6	123±6	117±5	115±7	125±4	122±5	117±4	118±5	122±6	121±11	126±9	106±9	121±23	117±6
933	118±6	122±6	119±6	116±6	123±5	119±5	122±5	121±4	120±6	119±8	125±7	110±11	147±21	118±6
1000	120±7	119±7	120±6	116±6	121±5	118±5	123±4	122±4	121±8	117±9	122±7	114±12	124±20	120±7
1067	120±6	117±7	121±7	115±8	122±5	118±5	122±5	122±4	123±8	117±8	124±8	114±10	124±11	120±6
1133	122±7	117±8	120±8	114±8	120±5	118±5	121±5	120±5	126±10	118±12	119±9	119±10	145±23	122±7
1333	122±6	117±6	118±8	118±7	122±5	117±5	121±5	118±5	126±9	125±12	120±8	119±8	129±24	122±6
1533	120±7	119±9	115±8	119±10	120±5	120±5	124±4	119±5	124±12	116±10	122±10	113±13	141±29	120±7
1733	120±8	121±8	117±7	121±6	121±5	119±5	123±4	118±5	122±11	117±10	124±10	110±6	138±26	120±8
1933	122±8	118±7	120±5	117±8	119±4	119±5	122±4	120±5	126±8	119±9	118±6	120±5	123±21	122±8
2133	123±6	116±6	121±5	116±7	120±4	119±4	120±5	119±5	126±10	115±10	120±8	117±7	147±14	123±6
2667	122±7	117±7	122±6	118±8	119±3	120±4	122±5	120±4	125±11	119±10	123±9	116±9	150±19	122±7
3667	114±6	122±5	120±5	118±7	127±2	118±5	115±2	119±4	119±8	124±5	124±14	120±17	109±19	114±6
4667	121±8	122±8	113±6	120±9	120±5	122±5	124±4	120±5	124±11	116±10	127±11	107±11	147±26	121±8
5667	118±7	119±7	124±8	108±9	126±4	120±6	115±2	119±5	122±9	124±10	122±13	110±9	112±16	118±7
10133	125±6	116±5	119±5	119±8	120±4	120±4	123±4	117±5	123±9	123±10	124±11	107±11	133±31	125±6
20133	114±5	129±6	112±8	117±11	125±4	123±4	121±6	122±3	125±7	121±11	127±9	106±12	119±31	114±5

Table S4 Genetic structural fitting results for dihedral angles. Uncertainty is calculated using one standard deviation of individual fitting results.

Time / fs	$\angle C_1C_2C_3C_4$	$\angle C_2C_3C_4C_5$	$\angle C_3C_4C_5C_6$	$\angle H_7C_3C_4C_5$	$\angle H_8C_4C_5C_6$	$\angle H_9C_5C_6C_1$	$\angle H_{10}C_6C_1C_2$	$\angle N_{11}C_1C_2C_3$	$\angle O_{14}C_2C_3C_4$	$\angle O_{12}N_{11}C_1C_2$	$\angle O_{13}N_{11}O_{12}C_1$	$\angle H_{15}O_{12}N_{11}C_1$	$\angle C_1C_2C_3C_4$
-4333	359±6	360±5	360±4	180±3	178±9	181±5	178±5	174±10	181±8	7±7	184±9	243±50	359±6
-4267	360±5	360±4	363±5	178±7	181±8	180±7	176±7	181±4	182±9	3±3	179±7	179±7	360±5
-333	360±3	361±3	359±4	182±4	180±2	182±8	180±2	178±6	180±6	4±5	183±4	179±3	360±3
-267	360±3	360±5	360±5	180±2	180±2	180±2	179±3	179±7	180±3	3±4	182±4	180±3	360±3
-200	360±8	360±6	360±7	180±3	180±7	179±7	180±5	178±15	180±14	8±9	183±3	172±29	360±8
-133	355±8	359±4	365±9	178±5	181±7	177±8	176±8	180±13	173±15	9±7	183±4	174±32	355±8
-67	364±9	361±10	354±15	176±8	177±6	181±9	182±8	178±11	188±12	23±11	176±6	165±27	364±9
0	367±9	361±6	348±10	173±5	178±8	187±5	175±5	175±7	179±7	27±18	181±8	206±31	367±9
67	366±10	359±8	354±10	175±5	178±7	187±5	177±4	178±9	182±10	16±7	179±8	179±40	366±10
133	356±11	360±9	360±9	178±6	181±9	180±8	178±7	175±8	182±12	18±24	191±8	196±32	356±11
200	360±8	360±6	359±10	182±5	181±9	180±5	178±6	180±8	180±10	14±9	188±6	197±29	360±8
267	363±7	359±5	357±6	186±4	181±8	174±5	181±7	177±17	181±5	21±8	189±7	163±18	363±7
333	362±9	357±7	356±11	184±7	177±7	177±6	177±7	183±19	184±12	19±12	187±11	162±27	362±9
400	361±13	358±10	359±21	179±8	180±9	179±8	182±8	178±14	185±21	21±28	184±16	171±20	361±13
467	360±9	362±12	360±22	181±8	178±9	181±9	183±8	183±14	182±16	25±42	181±12	178±23	360±9
533	359±12	359±15	366±20	181±8	179±9	180±8	180±9	179±18	185±26	45±69	187±11	181±42	359±12
600	357±18	359±17	364±19	178±8	182±8	182±8	180±8	179±24	184±35	158±92	185±19	175±101	357±18
667	364±20	359±19	359±20	182±8	181±8	180±8	180±7	178±22	193±38	161±92	183±19	188±66	364±20
733	362±20	360±24	362±27	180±8	179±8	179±8	182±8	177±31	192±39	185±96	179±24	178±60	362±20
800	361±19	359±19	359±23	184±7	182±9	180±9	181±8	184±29	183±28	156±74	185±22	181±60	361±19
867	359±21	361±23	359±19	181±8	182±8	180±9	180±8	182±29	178±27	162±66	181±23	171±50	359±21
933	362±17	358±14	363±14	180±8	181±8	182±8	179±8	180±21	183±22	171±78	177±19	179±84	362±17
1000	359±19	358±20	363±22	182±8	181±8	180±8	182±8	178±22	184±29	154±76	184±20	188±52	359±19
1067	360±21	359±27	365±23	179±8	181±7	180±8	179±8	183±26	181±33	161±78	186±20	196±46	360±21
1133	360±23	357±28	362±25	180±8	180±8	181±8	178±8	186±22	184±36	192±78	183±25	188±93	360±23
1333	362±26	358±26	360±25	181±8	180±8	180±8	179±7	181±20	173±59	190±77	183±21	187±62	362±26
1533	365±24	354±23	363±27	180±8	181±8	180±8	182±8	177±26	183±37	180±77	184±27	190±120	365±24
1733	360±18	363±20	355±23	181±8	179±8	181±8	180±8	185±22	178±36	173±91	185±19	189±101	360±18
1933	359±22	360±20	364±22	180±8	178±8	180±8	181±8	181±25	176±41	183±65	180±20	193±53	359±22
2133	362±22	358±21	362±20	180±8	181±7	181±8	179±8	181±28	183±33	177±75	182±22	192±72	362±22
2667	359±19	362±19	359±22	180±8	180±8	179±8	182±8	182±32	173±43	192±78	185±21	168±134	359±19
3667	362±15	356±17	361±16	181±9	183±8	179±9	180±8	185±28	181±27	167±80	183±20	185±45	362±15
4667	355±25	364±22	363±23	179±8	180±8	180±8	180±8	183±23	173±31	184±93	175±24	196±109	355±25
5667	358±16	362±21	361±20	181±8	180±9	181±8	180±9	177±29	178±28	181±89	182±25	182±60	358±16
10133	359±23	362±18	358±15	181±7	177±7	178±7	181±8	186±22	175±42	160±85	180±21	162±107	359±23
20133	365±23	355±23	363±17	181±8	180±8	182±8	179±8	177±20	187±20	175±88	182±21	186±106	365±23

9. Electronic structure validation

Through geometry optimization and minimal-energy conical intersection (MECI) search, we have identified two critical points relevant to the excited-state dynamics of o-nitrophenol: the Franck-Condon point geometry and the S_1/S_0 MECI. These points were used for benchmarking and active space determination of the electronic structure method to be used in dynamics.

We used the floating-occupation molecular orbital (FOMO) complete active space configuration interaction (CASCI) method (FOMO-CASCI) with a FOMO temperature β = 0.2 and a 2,2 active space (2 electrons in 2 orbitals) in TeraChem with the 6-31g** basis set.[7] The approach was validated against SA-2-XMS(0.2)-MR-CASPT2(2,2)/6-31g*[8] geometries and EOM-CCSD/cc-pVDZ[9] single-point energy calculations at the FOMO-CASCI-optimized geometries. A comparison of the energetics of the two relevant critical points at these three levels of theory (FOMO-CASCI, MS-CASPT2, and EOM-CCSD) are summarized in Fig. S6 and Tables S5, S6, and S7. The advantage of FOMO-CASCI is in its ability to treat S_0/S_1 MECIs (as opposed to single-reference methods such as TD-DFT and EOM-CCSD) and its relative stability and affordability compared to MS-CASPT2 and CASSCF. The absence of dynamic electron correlation results in an S_0/S_1 gap at the Franck-Condon point nearly 2 eV greater than determined from the experimental absorption spectra or predicted by either benchmark method when using FOMO(0.2)-CASCI(2,2). Nonetheless, the energetics for structural relaxation to the S_1/S_0 MECI are similar between the three methods. Our comparison of FOMO(0.2)-CASCI(2,2) to MS-CASPT2 and EOM-CCSD demonstrates the same qualitative relationships between different geometries key to the dynamics and suggests that dynamic electron correlation does not play a significant role in the outcomes we observe in AIMS dynamics using FOMO(0.2)-CASCI(2,2)/6-31g**.

Differences in the relaxation energy from the Franck-Condon geometry to the S_1/S_0 MECI across the different electronic structure methods, shown in Fig. S6, suggest that wavepackets described by the FOMO(0.2)-CASCI method should reach the S_1/S_0 MECI substantially faster than those described by MS-CASPT2 or EOM-CCSD. In fact, the energy difference between the Franck-Condon geometry and the S_1/S_0 MECI at the FOMO(0.2)-CASCI(2,2)/6-31g** level is approximately twice that of SA-2-XMS(0.2)-MR-CASPT2(2,2)/6-31g*. This overestimation by FOMO(0.2)-CASCI may be a large part of the rationale for the faster HONO rotation and consequent access of the S_1/S_0 MECI observed in AIMS compared to experiment (described in the main text).

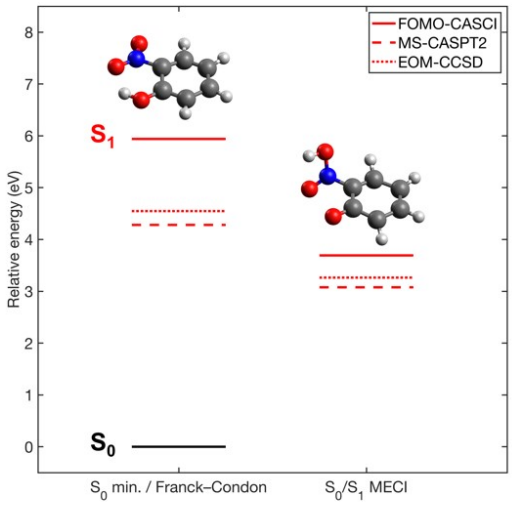

Fig. S6 Electronic structure validation. Critical points in the dynamics of o-nitrophenol calculated using FOMO(0.2)-CASCI(2,2)/6-31g**, XMS(0.2)-MR-CASPT2(2,2)/6-31g* and EOM-CCSD/cc-pVDZ electronic structure methods. The ground state Franck-Condon energy is taken as the zero of energy for each method.

Table S5 S_0 and S_1 energies for the S_0 minima and the S_0/S_1 MECI as calculated at the FOMO(0.2)-CASCI(2,2)/6-31g** level of theory.

State / Geometry	S_0 minimum / Franck-Condon	S_0/S_1 MECI
S0	-509.04727384	-508.90976736
S1	-508.82844840	-508.90976733

Table S6 S_0 and S_1 energies for the S_0 minima and the S_0/S_1 MECI as calculated at the SA-2-XMS(0.2)-MR-CASPT2(2, 2) / 6-31g* level of theory.

State / Geometry	S_0 minimum / Franck-Condon	S_0 / S_1 MECI
S0	-510.209491888592	-510.09518010
S1	-510.050822529609	-510.09482200

Table S7 S_0 and S_1 energies for the S_0 minima and the S_0/S_1 MECI as calculated at the EOM-CCSD / cc-PVDZ level of theory.

State / Geometry	S_0 minimum / Franck-Condon	S_0 / S_1 MECI
S0	-510.60215626	-510.50527406
S1	-510.43204238	-510.45619804

10. Potential energy surface and ionization potential along the reaction coordinate

To better understand the origin of the delay between proton transfer and access to the conical intersection, we have explored the $S_1(\pi\pi^*)$ potential energy surface topography between critical points along the reaction profile using electronic structure calculations. Fig. S7 shows the S_n (n=0,1) potential energy surfaces and ionization potential (IP) mapped *via* linear interpolation in internal geometric coordinates (LIIC). The LIIC comprises two separable coordinates: (i) the proton-transfer coordinate connecting the Franck-Condon point to an *aci*-nitro $S_1(\pi\pi^*)$-state local minimum-energy geometry (a coordinate dominated, by an increase and decrease in $r\mathrm{O_CH}$ and $r\mathrm{O_NH}$, respectively); and (ii) the HONO torsional coordinate connecting the *aci*-nitro $S_1(\pi\pi^*)$-state local minimum-energy geometry to the S_1/S_0 CI (a coordinate dominated explicitly by an increase in *d*ONCC). The change in gradient around the *aci*-nitro $S_1(\pi\pi^*)$-state local minimum-energy geometry (described in Table S8) slows down the nuclear wavepacket (potentially trapping part of it temporarily behind a small barrier) as the HONO torsional coordinate is accessed, therefore delaying access to the conical intersection.

All complete active space self-consistent field (CASSCF) and similarity-transformed equation-of-motion coupled cluster (STEOM-CCSD) calculations were carried out using ORCA (v4.2.1).[10]

The CASSCF active space comprised two electrons distributed over two orbitals – the highest-energy occupied (HOMO) and lowest-energy unoccupied (LUMO) π and π* orbitals – both of A″ symmetry - respectively. State averaging was carried out over the two lowest-energy singlet states – the electronic ground state (S_0; A′ symmetry) and the first electronically-excited singlet state {$S_1(\pi\pi^*)$; A′ symmetry}. These calculations are denoted SA2-CASSCF(2,2) throughout.

The STEOM-CCSD calculations used the back-transformed (bt) pair natural orbital (PNO) implementation in ORCA to accelerate the CCSD calculation of the reference state with the domain-based local PNO (DLPNO) strategy. These calculations are denoted bt-PNO-STEOM-CCSD throughout. The cc-pVDZ basis set was used throughout. All critical points on the S_n (n = 0, 1) potential energy surfaces were optimized at the SA2-CASSCF(2,2) level. C_s-symmetric S_0-state and $S_1(\pi\pi^*)$-state minimum energy geometries were located and verified *via* vibrational frequency analysis. The C_1-symmetric S_1/S_0 minimum-energy crossing point (MECP, or conical intersection; CI) was located *via* a home-built external optimizer following the penalty-constrained approach of Martinez *et al*.[11] S_n (n = 0, 1) energies were reevaluated at these geometries at the bt-PNO-STEOM-CCSD level. The energies of the S_n (n = 0, 1) states were reevaluated at the bt-PNO-EOM-CCSD level at each interpolated position; at the S_1/S_0 MECP, the energies of both states were averaged to account for their non-degeneracy when evaluated with bt-PNO-STEOM-CCSD at the SA2-CASSCF(2,2)-optimized geometry.

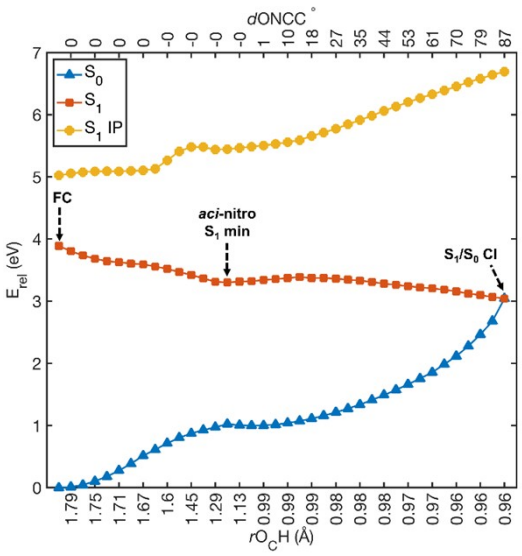

Fig. S7 Plot showing the Sn (n = 0, 1) potential energy surface scans at the bt-PNO-STEOM-CCSD/cc-pVDZ level between the Franck-Condon point (the S0-state minimum-energy geometry) and the *aci*-nitro $S_1(\pi\pi^*)$ minimum [$S_1(\pi\pi^*)$ state], *i.e.* the proton transfer coordinate, and between the *aci*-nitro $S_1(\pi\pi^*)$ minimum and the S_1/S_0 CI [S1($\pi\pi^*$) state], the dominant structural change here being HONO torsion. The energy of the S_1 and S_0 states are shown as orange squares and blue triangles, respectively. The ionization potential calculated at every point of the scan is shown as the yellow circles.

Table S8 *Aci*-nitro $S_1(\pi\pi^*)$-state local minimum-energy geometry optimized at the SA2-CASSCF(2,2) level of theory.

Cartesian coordinates / Å	15			
	C	0.00000	0.00000	0.00000
	C	1.40310	0.00000	0.00000
	C	2.10732	0.00000	1.18935
	C	1.41070	-0.00276	2.39934
	C	0.01768	-0.00489	2.42731
	C	-0.70996	-0.00280	1.23196
	N	-0.67562	0.00085	-1.22288
	O	-0.11002	0.01921	-2.30493
	O	-2.02932	-0.01492	-1.27258
	O	-2.02103	-0.00041	1.18527
	H	1.89575	-0.00221	-0.97444
	H	3.19874	0.00033	1.17640
	H	1.95500	-0.00444	3.34706
	H	-0.53644	-0.00543	3.36653
	H	-2.38270	-0.02569	-0.34850

11. Potential energy surface scan along the IPT coordinate

To better understand the role of the donor-acceptor compression in the IPT of o-nitrophenol, we calculated the S_1 energy along the IPT coordinate, as shown in Fig. S8. Energy traces along two IPT coordinates are shown: at a fixed equilibrium donor-acceptor distance (blue line) and along a minimum energy path where there is transient compression of the donor-acceptor distance from 2.55 to 2.37 Å (orange line). These calculations, performed at the SA2-CAS(2,2)/cc-pVDZ level of theory, show that the transient compression of the donor-acceptor separation (rO_CO_N) lowers the energy barrier along the proton transfer coordinate significantly.

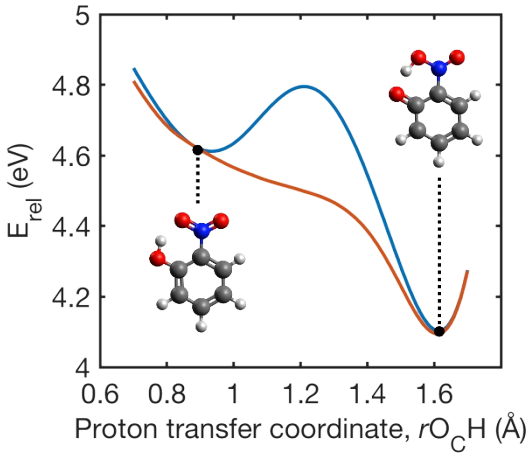

Fig. S8 Plot showing the S_1 energy across the IPT coordinate: at a fixed equilibrium donor-acceptor distance (blue) and along the minimum-energy path (orange) involving a transient compression of the (rO_CO_N) donor-acceptor distance from 2.55 to 2.37 Å [SA2-CAS(2,2)/cc-pVDZ]. The insets on panel (b) show the geometries of o-nitrophenol before and after IPT.

12. Potential energy surface scan along the IPT coordinate

Generalized Ab Initio Multiple Spawning simulations were carried out on a subset of initial conditions to investigate a potential decay pathway through ultrafast intersystem crossing via triplet states. To accommodate the relevant triplet states, the active space was extended by using the FOMO(0.2)- CASCI(4,3) / 6-31g** electronic structure method. These simulations confirmed that the spin-orbit couplings between singlet and triplet manifolds are too weak to strongly impact the short time-scale dynamics. Figure S9 shows the T_1 triplet population as a function of time observed when spawning thresholds are set to force spawning with encountered spin orbit coupling values. Further studies would, however, be required to determine the role of intersystem crossing at much longer timescales.

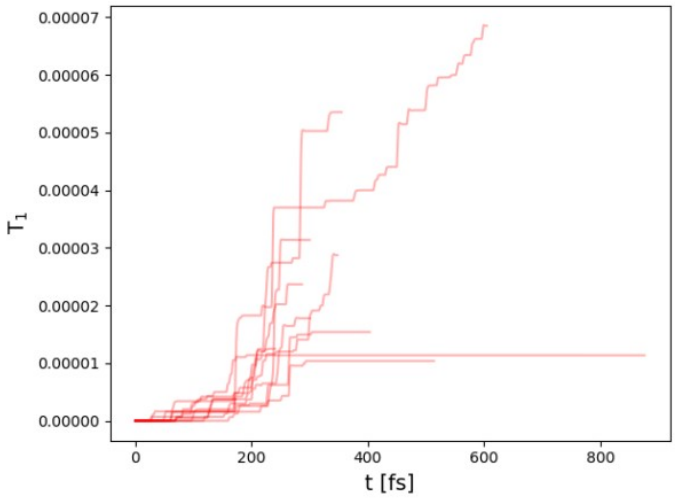

Fig. S9 Population of T_1 triplet surface with spawning thresholds set to force spawning with encountered spin orbit coupling values.

13. Excitation efficiency estimation

The excitation efficiency is estimated as the ratio between the amplitude of the average experimental difference diffraction signal between 0.75 and 1 ps and the average theoretical difference signal over the same time window. The theoretical difference signal is calculated based on AIMS simulations, which inherently assume 100% excitation efficiency. The resulting scaling factor between experiment and theory serves as a rough estimate of the percentage of molecules in the probed volume which have undergone photoexcitation by the pump laser pulse.

References

1 J. S. Baskin and A. H. Zewail, *ChemPhysChem*, 2005, **6**, 2261–2276.

2 F. Salvat, A. Jablonski and C. J. Powell, *Computer Physics Communications*, 2005, **165**, 157–190.

3 H. Ihee, B. M. Goodson, R. Srinivasan, V. A. Lobastov and A. H. Zewail, *Journal of Physical Chemistry A*, 2002, **106**, 4087–4103.

4 H. Ihee, J. Cao and A. H. Zewail, .

5 S. Habershon and A. H. Zewail, *Chem. Eur. J. of Chem. Phys.*, 2006, **7**, 353–362.

6 J. Yang, X. Zhu, J. P. F. Nunes, J. K. Yu, R. M. Parrish, T. J. A. Wolf, M. Centurion, M. Gühr, R. Li, Y. Liu, B. Moore, M. Niebuhr, S. Park, X. Shen, S. Weathersby, T. Weinacht, T. J. Martinez and X. Wang, *Science*, 2020, **368**, 885–889.

7 P. Slavíček and T. J. Martínez, *The Journal of Chemical Physics*, 2010, **132**, 234102.

8 J. Finley, P.-Å. Malmqvist, B. O. Roos and L. Serrano-Andrés, *Chemical Physics Letters*, 1998, **288**, 299–306.

9 T. Korona and H.-J. Werner, *The Journal of Chemical Physics*, 2003, **118**, 3006–3019.

10 F. Neese, *WIREs Comput Mol Sci*, 2012, **2**, 73–78.

11 B. G. Levine, J. D. Coe and T. J. Martínez, *Journal of Physical Chemistry B*, 2008, **112**, 405–413.